

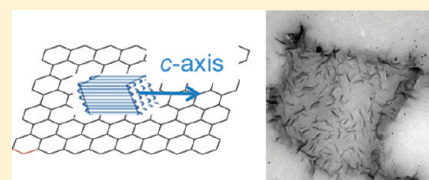
Reduced Graphene Oxide-Induced Polyethylene Crystallization in Solution and Nanocomposites

Shan Cheng,[†] Xi Chen,[†] Y. Grace Hsuan,[‡] and Christopher Y. Li^{*,†}

[†]Department of Materials Science and Engineering, Drexel University, Philadelphia, Pennsylvania 19104, United States

[‡]Department of Civil, Architectural and Environmental Engineering, Drexel University, Philadelphia, Pennsylvania 19104, United States

ABSTRACT: We report epitaxial crystallization of polyethylene (PE) on reduced graphene oxide (RGO) nanosheets via a controlled solution crystallization method. Polarized light microscopy, scanning electron microscopy, transmission electron microscopy, and atomic force microscopy were used to investigate morphology of RGO-induced PE crystals. The PE edge-on crystals formed from randomly distributed rodlike nuclei on the basal plane of RGO nanosheets and further grew into larger lamellae with an average dimension of a few hundreds of nanometers. Selected area electron diffraction (SAED) pattern revealed that the *c*-axis of polymer chain is parallel to the basal plane of the RGO nanosheets. PE/RGO nanocomposites (PGNs) with different RGO loadings were fabricated through solution crystallization/precipitation using the PE-decorated RGO hybrid as the precursor. Both nonisothermal and isothermal crystallization behaviors of PGNs were studied using differential scanning calorimetry (DSC). Crystallization kinetics of PGNs was substantially accelerated in the presence of 2D RGO nanosheets. Dramatic improvement of thermal stability was found for PE in the presence of a small amount of RGO nanosheets.



INTRODUCTION

Since the discovery in 2004 by Novoselov et al.,¹ graphene has drawn a great deal of interests in various applications due to its unique electrical,^{1–3} thermal,^{4,5} and mechanical^{6,7} properties. One of the most attractive applications of graphene is polymer nanocomposites, where graphene is often employed in different forms such as graphene oxide (GO) and chemically or thermally reduced graphene oxide (RGO).⁸ The pioneer work on polystyrene/graphene nanocomposites by Ruoff et al. showed extraordinary electrical properties with percolation occurring at 0.1 vol % of graphene loading.⁹ Extensive research on different polymer/graphene nanocomposites systems with enhanced properties has been conducted afterward; polymers that have been used include thermoplastics such as poly(vinyl alcohol),^{10–12} polyamide 6,¹³ poly(L-lactide),¹⁴ thermosets such as epoxy,^{15,16} elastomers such as polyurethanes,^{17,18} amorphous glassy polymers such as polystyrene,^{9,19} poly(methyl methacrylate),²⁰ and functional polymers such as polyaniline^{21,22} and poly(3-hexylthiophene).²³

Semicrystalline polymer is one of the most important matrices that used in polymer nanocomposites. Study of the crystallization behavior of semicrystalline polymer nanocomposites is of both scientific and practical importance because crystal structure and morphology are directly related to the properties of the material such as mechanical strength. Nanosized fillers such as 1D carbon nanotubes (CNTs)^{24–30} and 2D nanoclay^{31–34} are known to enhance the heterogeneous crystallization of the crystalline polymer matrix. Graphene, which exhibits a 2D geometry as nanoclay, and has sp² carbon atoms arranged in a hexagonal lattice as CNT, has also been considered to have great impact on the crystallization behavior

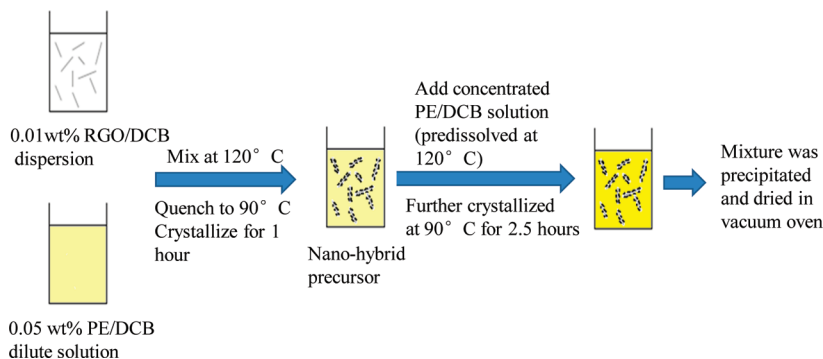
of polymer nanocomposites. Xu et al. compared the geometric effects of both CNT and graphene nanosheets (GNS) on the crystallization kinetics of poly(L-lactide) (PLLA). In general, the half-crystallization time ($t_{1/2}$) was significantly shortened for PLLA/CNT and PLLA/GNS nanocomposites compared with neat PLLA. However, the induction time was shortened when the CNT loading increased from 0.05 to 0.1 wt %, whereas the inverse trend is found in GNS system.¹⁴ Their further work on isotactic polypropylene (iPP)/GNS nanocomposites showed that the $t_{1/2}$ was reduced to more than 50% for 0.05 wt % iPP/GNS nanocomposites compared to neat iPP under quiescent condition. Crystallization kinetics become even faster under shear flow.³⁵ A few studies on poly(vinyl alcohol) (PVA)/RGO nanocomposites have shown an increased glass-transition temperature (T_g) due to the restriction of polymer chain motion by the H-bonding interaction between PVA chains and the filler.^{10–12} Both Yang et al.¹¹ and Salavagione¹² report a significant reduction of crystallinity from around 50% of neat PVA to almost amorphous phase at high graphene content, which compromises the mechanical properties of the nanocomposites. However, Liang et al.¹⁰ report no obvious change in crystallinity and melting temperature but a 76% increase in tensile strength and a 62% increase in Young's modulus for 0.7 wt % nanocomposites. They ascribe this improvement to the molecular level dispersion of graphene in the polymer matrix and the efficient load transfer due to strong interfacial interactions.

Received: September 22, 2011

Revised: November 18, 2011

Published: December 22, 2011

Scheme 1. Fabrication Process of PE/RGO Nanocomposites



Polyethylene (PE)/graphene nanocomposites have been studied very recently by Kim et al., and they found that linear low-density polyethylene samples modified with different polar functional groups such as $-\text{NH}_2$, $-\text{NHEt}$, $-\text{CN}$, and $-\text{NCO}$ are more compatible with graphene and have higher tensile modulus compared with the unmodified PE.³⁶ At the same time, molecular dynamics (MD) simulations of PE nanocomposites system with different nanofillers (buckyball, graphene, single wall carbon nanotubes) showed that graphene sheets have the strongest interaction with PE matrix among all the nano inclusions.³⁷

In this article, we report the study of crystallization behavior of a PE/RGO system. First, epitaxial crystallization of PE crystals on the basal plane of RGO sheets was observed from controlled solution crystallization. The morphology of PE lamellae was clearly revealed by transmission electron microscopy (TEM) and atomic force microscopy (AFM), and the orientation of the polymer chain was determined by selected area electron diffraction (SAED). PE/RGO nanocomposites (PGNs) with different RGO loadings were further prepared through a coprecipitation method. Crystallization behaviors from the melts of nanocomposites as well as the thermal stability were investigated and discussed. This study will shed light on better understanding of the influence of 2D graphene sheets on the crystallization behavior of semicrystalline polymer nanocomposites and on fabricating advanced hybrid materials with improved mechanical properties as well as other functionalities.

EXPERIMENTAL SECTION

Materials and Methods. Natural flake graphite with an average lateral size of $\sim 44 \mu\text{m}$ was kindly provided by Asbury Carbons, Inc. High-density PE pellets ($M_w = 125\,000$, $\rho = 0.95 \text{ g/cm}^3$, melt flow index = 0.3 g/10 min) were purchased from Scientific Polymer Products. Hydrochloric acid (HCl) (37%), sulfuric acid (H_2SO_4) (95–98%), potassium permanganate (KMnO_4) ($\geq 99.0\%$), sodium nitrate (NaNO_3) ($\geq 99.0\%$), hydrogen peroxide (H_2O_2) (35%), hydrazine hydrate ($\text{N}_2\text{H}_4\cdot\text{H}_2\text{O}$) (50–60%), 1,2-dichlorobenzene (DCB) (spectrophotometric grade, 99%), and N,N' -dimethylformamide (DMF) were purchased from Sigma-Aldrich and used as received.

RGO was prepared using a chemical oxidation–reduction process. First, graphite oxide was synthesized by the modified Hummers method.^{13,38} Graphite (1.0 g), NaNO_3 (0.5 g), and KMnO_4 (3.0 g) were loaded into a 50 mL flask and cooled in an ice bath, followed by slow addition of 25 mL of H_2SO_4 under stirring. The mixture was then heated to 35°C in an oil bath with continued stirring for 2 h. The product was poured into excess deionized (DI) water and cooled in an ice bath. H_2O_2 was slowly added until no gas evolution was observed. The product was then filtered, washed with 5% HCl solution, and DI water, and subsequently dried in a vacuum oven at room temperature

over 1 week. RGO nanosheets were then obtained by chemical reduction of GO using hydrazine hydrate as the reductant.^{39,40} GO (75 mg) was first dispersed in 80 mL of DMF/water (volume ratio 9:1) mixed solution via sonication, followed by reacting with 3 mL of hydrazine hydrate at 100°C for 24 h under stirring to yield a homogeneous suspension of RGO sheets.

Epitaxial crystallization of PE on RGO nanosheets was achieved via a controlled solution crystallization procedure.²⁶ RGO (1 mg) was dispersed in 10 mg of DCB by sonication for 1–2 h to form a uniform dispersion of single-layer or a few-layer RGO sheets, which was then mixed with 10 mg of 0.05 wt % predissolved PE/DCB solution at 120°C . The mixture was quenched to 90°C and crystallized for 1 h, followed by isothermal filtration at 90°C to remove excess free polymer. This resulted in a nanohybrid structure with RGO nanosheets decorated with PE single crystals on both surfaces that are ideal for morphological and structural study. PE/RGO nanocomposites (PGNs) can be further fabricated using this nanohybrid structure as the precursor. Instead of isothermal filtration, concentrated PE/DCB solutions with desired weight percentages were added into the precursor and further crystallized for 2.5 h at 90°C . The mixture was then coprecipitated in excessive methanol dropwise, filtered, washed with methanol to remove residual solvent, and dried in vacuum oven at room temperature for 1 week (Scheme 1).

Characterization. Differential scanning calorimetry (DSC) experiments were carried out using a Perkin-Elmer DSC 7. The samples with an average weight of 2–4 mg were heated from 30 to 200°C at a scanning rate of 10°C/min under a nitrogen atmosphere and were cooled and reheated using the same rate. 100% crystallized PE with an enthalpy of fusion of 293.6 J/g was used as a reference to calculate the crystallinity of the nanocomposites samples. Isothermal crystallization was conducted by quenching samples from 200°C to the preset crystallization temperatures at 400°C/min . Thermogravimetric analysis (TGA) tests were performed using a Perkin-Elmer TGA 7 under nitrogen atmosphere with 20 mL/min flow rate. Approximately 3–5 mg of sample was heated from 30 to 650°C at a heating rate of 10°C/min . Tapping mode AFM experiments were conducted using a Nanoscope IIIa (Digital Instruments/Veeco). Sample was spin-coated on a clean glass slide and dried in a vacuum oven before test. TEM characterization was conducted by a JEOL JEM2100 microscope with an accelerating voltage of 200 kV. Samples were spin-coated on carbon-coated copper grids and dried in a vacuum overnight. Scanning electron microscopy (SEM) experiments were performed using a Zeiss Supra 50VP scanning electron microscope. Samples were spin-coated onto a glass slide, vacuum-dried to remove solvent, and sputtered with platinum for 25 s before testing. Wide-angle X-ray diffraction (WAXD) experiments were conducted using a Siemens D500 diffractometer with a $\text{Cu K}\alpha$ wavelength of 1.54 \AA . Samples were scanned from 5° to 40° at a rate of $0.03^\circ/\text{s}$. Morphology of PGN was also investigated using a polarized light microscope (PLM) (Olympus BX51) equipped with a Mettler Toledo hot stage (MTFP82HT). Elemental analysis and Karl Fischer coulometric titration were conducted in Robertson Microlit Laboratories (Ledgewood, NJ).

RESULTS AND DISCUSSION

Characterization of RGO Nanosheets. The chemical oxidation–reduction reaction of graphite provides an easy and feasible way to obtain single- or few-layer graphene nanosheets at a large scale. Figure 1a shows a typical TEM micrograph of

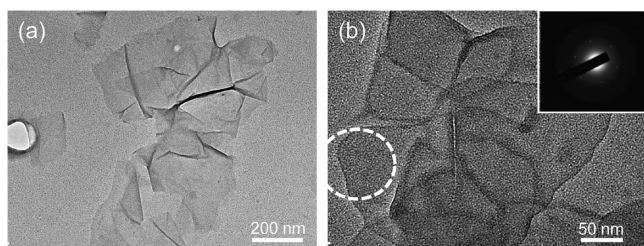


Figure 1. TEM micrographs of RGO sheets. (a) RGO deposited on carbon-coated Cu grid. (b) Higher magnification of one layer of RGO and the corresponding SAED pattern of the circled region.

RGO sheets made by sonication of reduced graphite oxide in DCB for 1 h. These sheets have an average lateral size of 0.2–1 μm and partially overlap with each other. Buckling of the sheets is evident, particularly in the overlapped regions. The SAED pattern from the dotted circle area (Figure 1b) shows a typical hexagonal symmetry, which is representative for graphene layers. Thermal stability tested by TGA (Figure 2) shows the

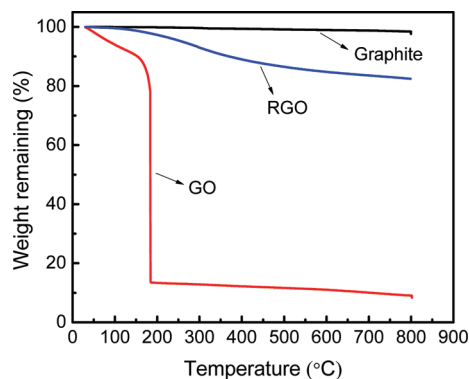


Figure 2. TGA of pristine graphite, GO, and RGO.

synthesized RGO retained 83% in weight after being heated to 800 $^{\circ}\text{C}$, while GO lost more than 80% weight near 200 $^{\circ}\text{C}$. These results are comparable with literature values.³⁹ Elemental analysis together with Karl Fischer coulometric titration shows that the C/O molar ratio increases from 1.3 for GO to around 6 for RGO, indicating the removal of the functional groups and recovery of sp^2 carbon bond of GO after chemical reduction.

RGO-Induced PE Crystallization in Dilute Solution. It has been demonstrated that graphite can induce polymer epitaxial crystallization. Balik et al. observed epitaxial growth of polyoxymethylene (POM) from 0.5% iodobenzene solution onto the basal plane of graphite substrate to form a rodlike structure well oriented in three directions.⁴¹ Early work of epitaxial growth of polyamide on graphite revealed that the polymer chain adopted an all-trans conformation and interacted with adjacent chains through hydrogen bonding.⁴² The first study of PE crystallization on graphite was conducted in the 1970s, when the epitaxial relation $(0001)\langle 2-1-10 \rangle_{\text{graphite}} // (110)\langle 001 \rangle_{\text{PE}}$ was reported.⁴³ More recent research by Takenaka et al. confirmed the crystallization of PE on highly

oriented pyrolytic graphite (HOPG) to be indeed epitaxial, and they further found that the monoclinic phase instead of orthorhombic phase was formed at the interface.⁴⁴

In the present work, controlled solution crystallization²⁶ has been used to study the crystallization of PE on RGO nanosheets. Epitaxial growth of PE crystals on RGO occurs over a broad range of temperatures. Figure 3a shows PE

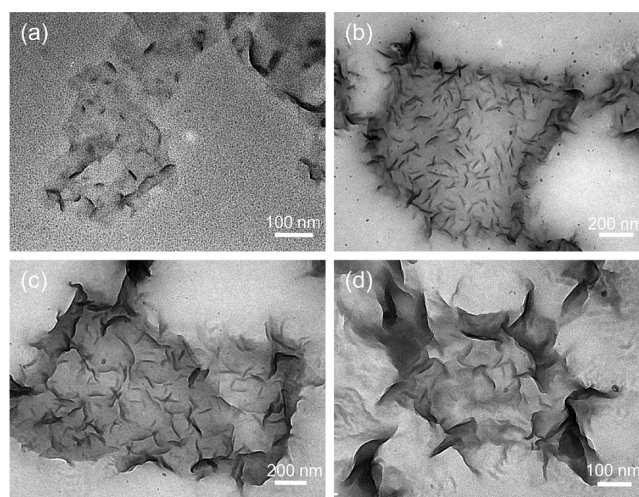


Figure 3. Bright-field TEM images of RGO nanosheets induced PE crystallization at different conditions. (a) PE was crystallized at 90 $^{\circ}\text{C}$ for 1 h with a PE/RGO concentration ratio of 1:2. (b–d) PE was crystallized at 100 $^{\circ}\text{C}$ overnight with PE/RGO ratio 1:1, 2:1, and 5:1, respectively.

crystallized at 90 $^{\circ}\text{C}$ for 1 h with a PE/RGO concentration ratio of 1:2. Discrete nuclei and small rodlike crystals can be observed on the surface of RGO nanosheets, which represents the early stage of PE crystallization. Figure 3b–d shows PE crystallization at 100 $^{\circ}\text{C}$ overnight with PE/RGO ratio of 1:1, 2:1, and 5:1, respectively. Small nuclei and crystals of PE continue grow into larger lamellae with an average size of 100 nm when increasing the crystallization time. And as the PE/RGO concentration ratio increases, these edge-on lamellae can further grow, and above a certain degree, the lamellae start to bend and orientation of the lamellae at the crystal/RGO interface becomes less clear (Figure 3c,d). Tapping mode AFM experiments were conducted on PE/RGO hybrids crystallized at 100 $^{\circ}\text{C}$ overnight with PE/RGO ratio of 1:1. RGO is covered with PE crystals (Figure 4a). The height of PE edge-on crystals ranges from several nanometers to a few tens of nanometers (Figure 4b, green arrows). The vertical distance between the RGO flake surface and the substrate (red arrows in Figure 4b) is around 13 nm, which suggests that PE crystals are grown on both sides of the RGO sheets.

The orientation of polymer chains is determined by SAED. Figure 5a shows PE crystal-decorated RGO while Figure 5b shows the corresponding SAED pattern with the correct orientation. In the diffraction pattern, the bright spots are diffractions from RGO, and the arcs with weaker intensity are diffractions from PE. Six symmetric PE (002) reflection arcs are superimposed with RGO (2–1–10) reflections, and the (310) PE diffraction can be found close to (10–10) RGO diffractions. These indicate the c -axis of polymer is parallel to the basal plane of RGO sheets, and the PE crystals are preferentially growing at three directions that are 120 $^{\circ}$ apart from each other. The overlapped PE and RGO diffraction patterns are consistent

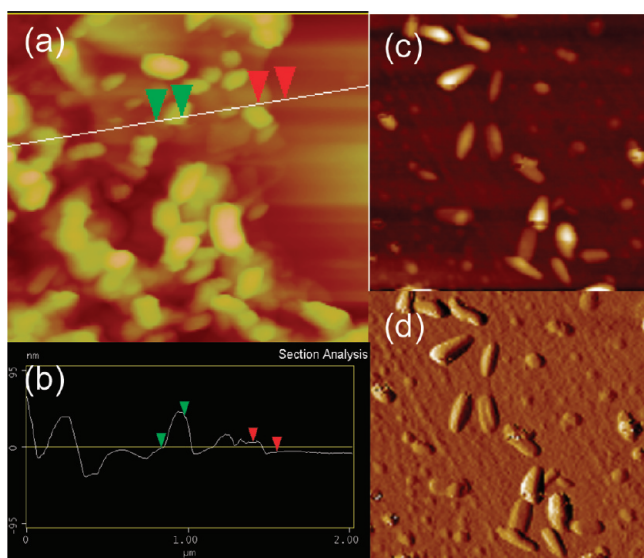


Figure 4. Tapping mode AFM images of PE crystals on RGO sheets. (a) is the height image of a 2 μm scan, and (b) is the corresponding height profile along the white line in (a). (c) and (d) are height and amplitude images, respectively, at a higher magnification (0.8 μm scan). Sample was taken from the same batch in Figure 3b.

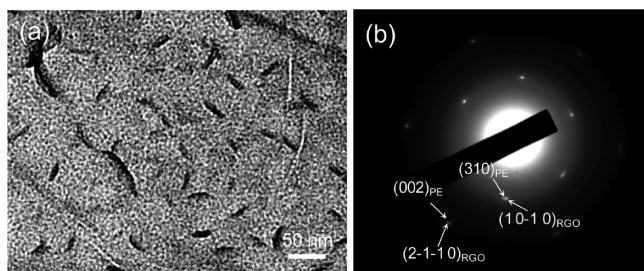


Figure 5. (a) High-magnification TEM image of PE single crystal epitaxially grown on RGO sheets; PE/RGO concentration ratio 1:1. (b) The corresponding SAED pattern.

with earlier work,^{43,44} suggesting an epitaxial relation of $(0001)\langle 2-1-10 \rangle_{\text{RGO}} // (110)\langle 001 \rangle_{\text{PE}}$.

As a control experiment, PE was also crystallized on the pristine graphite flakes in the same way as PE/RGO system. Figure 6a reveals that PE lamellae have densely grown on the

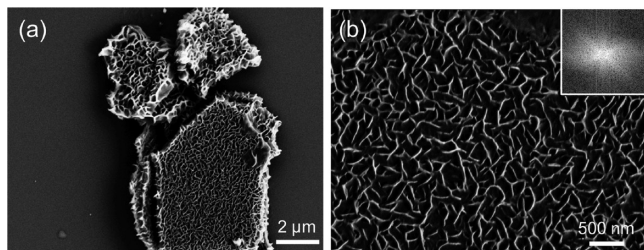


Figure 6. SEM image of (a) PE crystallization on graphite flake surface, graphite/PE concentration ratio 1:5, crystallized for 1 h at 90 $^{\circ}\text{C}$. (b) Higher magnification image of (a). Inset shows a fast Fourier transform of the image.

(001) surface of the pristine graphite with edge-on orientation, and the lamellae size is ~ 200 nm. The PE crystals appear to be more uniform with a larger crystal size on pristine graphite compared with RGO, which is probably due to the larger lateral

size (2–10 μm) and less defect sites of graphite flakes compared with RGO. Fast Fourier transform (FFT) shows stronger scattering in two directions while relatively weak scattering in the third direction, which may be because of local preferred orientation of PE lamellae along two directions.

Crystalline Morphology of PGNs. PGNs with seven different RGO loadings ranging from 0.04 to 4.4 vol % were prepared according to the method discussed in the Experimental Section. The volume fraction was converted from weight fraction using the density of 0.95 and 2.2 g/cm^3 for PE and RGO, respectively. WAXD was used to study the crystalline structure of these PGNs (Figure 7). Two peaks at

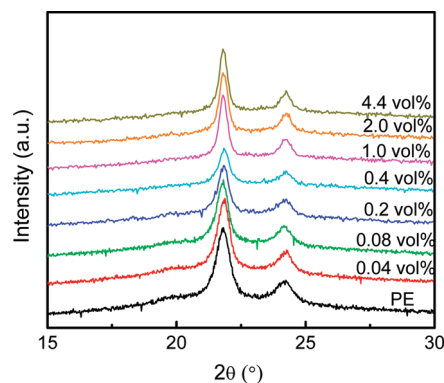


Figure 7. WAXD patterns of PE/RGO nanocomposites.

$2\theta = 21.78^{\circ}$ and 24.23° were observed for all PGNs, which correspond to the (110) and (200) Bragg reflections of PE, respectively. The intensity ratio of (110) and (200) peaks remains unchanged for all the PGNs, indicating that the addition of RGO nanosheets does not significantly modify the crystalline morphology of PE.

PGN films were melted at 160 $^{\circ}\text{C}$ and quenched to 115 $^{\circ}\text{C}$ crystallization temperature for polarized light microscopy (PLM) evaluation. Figure 8 shows that large agglomerates are absent in the PGN samples, indicating good dispersion of RGO sheets in the polymer matrix. In contrast with neat PE, which consists of large spherulites, all the PGN samples show a reduced crystalline size. This is common in most polymer nanocomposites systems since the presence of RGO network significantly restricts the 3D growth of polymer spherulites.⁴⁵

Crystallization Behavior of PGNs. The influence of 2D RGO sheets on the crystallization behavior of PGNs is of interest. Both nonisothermal and isothermal crystallization behaviors of PGNs were studied by DSC. Figure 9 shows the nonisothermal crystallization/melting behavior of PGNs with different RGO loadings. The first heating curve represents the thermal history of PGNs and is strongly influenced by the fabrication process, while the second heating curve reveals the crystallization of PGNs from melts. An intriguing observation is that two distinct melting peaks are observed on the first heating curves of 0.04 and 0.08 vol % PGNs, while PE only has a single melting peak (Figure 9a). The relative intensity of the peak with higher T_m increased as the RGO content increased, whereas the peak with lower T_m diminished and broadened with the increase of RGO content. The melting peak with higher T_m can be explained as a result of the heterogeneous nucleated, better formed PE crystals templated by the RGO sheets during solution crystallization. The increase of RGO concentration provides more sites for polymer to nucleate and

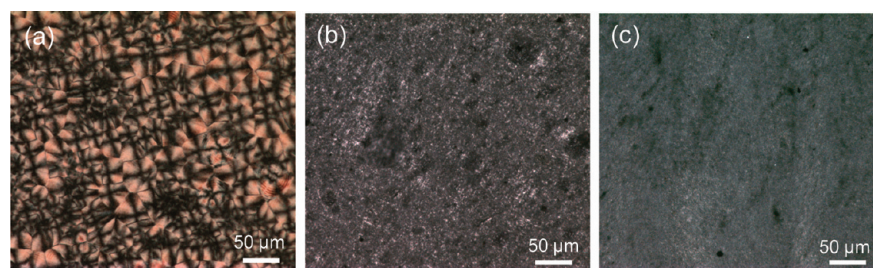


Figure 8. PLM micrographs of (a) neat PE and nanocomposites containing (b) 0.04 vol % and (c) 0.2 vol % of RGO.

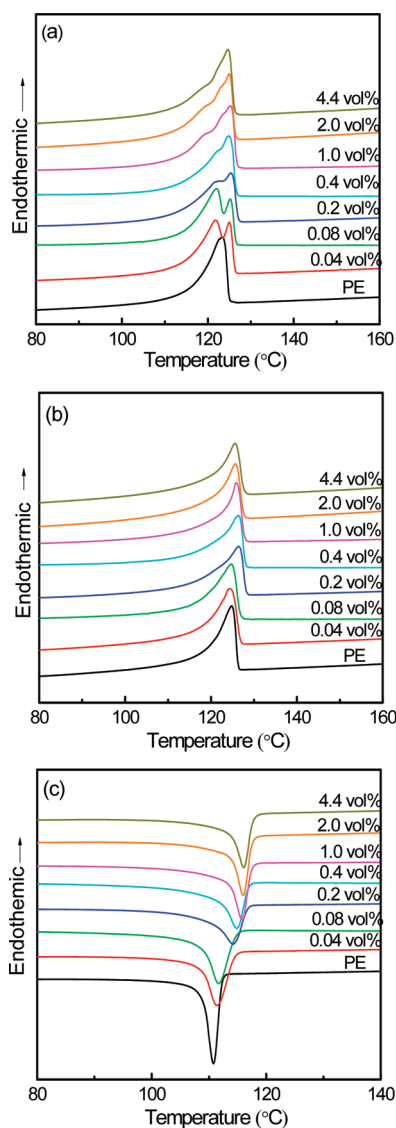


Figure 9. Nonisothermal DSC scans of PGNs at a constant scanning rate of 10 °C/min: (a) first heating, (b) second heating, and (c) cooling.

grow and thus contributes to higher intensity of the melting peak. During the second heating process in DSC, the crystallization became more uniform in melt, and all PGNs exhibited only one single melting peak (Figure 9b).

The melting temperature T_m determined by the second heating is summarized in Table 1. There is 1–1.5 °C variation of T_m for different samples, but in general the addition of RGO does not significantly alter the T_m of PGNs. The crystallization

Table 1. Crystallization Characteristics of PGNs with Different RGO Contents

RGO (vol %)	T_c (°C)	first heating		second heating	
		T_m (°C)	crystallinity (%)	T_m (°C)	crystallinity (%)
PE	110.8	123.3	53.7	124.9	58.9
0.04	111.5	121.9/125.0	57.8	124.4	58.5
0.08	111.6	122.0/125.3	59.4	124.7	59.5
0.2	114.3	125.4	56.7	126.4	57.2
0.4	114.8	124.8	60.2	126.4	58.6
1.0	115.8	125.2	70.1	125.9	60.7
2.0	116.0	125.0	70.4	125.7	60.4
4.4	116.1	124.7	72.4	125.5	61.6

temperature (T_c) which obtained from the exothermic peak on the DSC cooling curve (Figure 9c) increased from 110.8 °C of pure PE to 116.1 °C of 4.4 vol % PGN (Table 1). This dramatic increase of T_c was attributed to the heterogeneous nucleation induced by the 2D RGO nanosheets.

Crystallinity data determined from the heat of fusion under the area of melting peaks for PGNs are shown in Table 1. All the crystallinity calculation for PGNs was normalized by PE weight. According to the second heating data, the addition of RGO does not change much of the crystallinity (from 58.9% to 61.6%). However, most of the PGN crystallinity calculated from first heating data is higher than that from second heating, and this trend becomes more prominent at higher RGO loadings (above 0.4 vol %). This further confirms that PE crystals induced by RGO are better ordered so that as the RGO contents increase, the percentage of RGO-induced PE crystal increases, leading to a higher crystallinity. A similar phenomenon was observed for PE/CNT system using the nanohybrid shish kebab as template.²⁴

Isothermal crystallization of PGNs at low RGO loadings was also investigated by DSC. Figure 10a shows the results of PGNs up to 0.4 vol % that crystallized at 117 °C. $t_{1/2}$, which is defined as the time taken to complete 50% of the crystallization process, is plotted in Figure 10b. At higher RGO loading, the crystallization of PGNs becomes even faster than the isothermal peaks are no longer distinguishable under present crystallization conditions and therefore was not discussed here. A broad exothermic peak was observed for PE while the peak becomes much narrower for all the PGN samples. The $t_{1/2}$ decreases to ~27% of pure PE at 0.04 vol % of RGO loading and ~11% of pure PE at 0.4 vol % of RGO loading, indicating the efficient nucleation ability of RGO nanosheets. This acceleration effect of the nanofiller on the crystallization kinetics of polymers is common in most of the PE/CNTs,^{24,28} PE/nanoclay systems,³² and iPP/graphene systems.³⁵ However, contradictory results were observed in some nylon/MWNT²⁵ as well as PLLA/

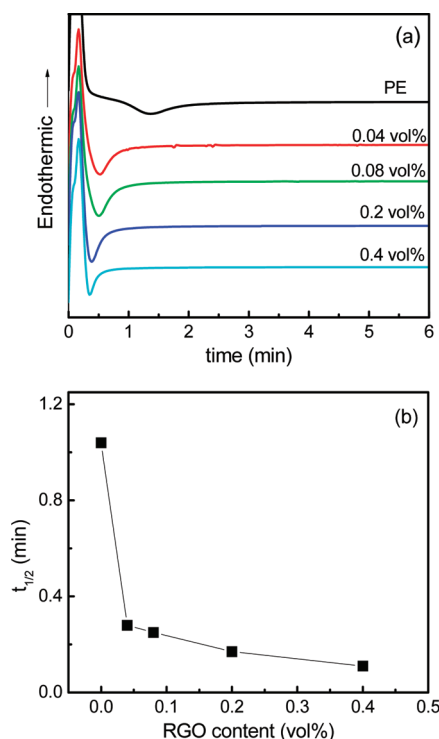


Figure 10. Isothermal crystallization behavior of PGNs. (a) DSC curves of PGNs crystallized at 117 °C. (b) Plot of $t_{1/2}$ against RGO contents.

graphene nanosheets system,¹⁴ in which the crystallization was initially accelerated and then hindered as further increasing the nanofiller loading. The latter results suggest complex effects of CNT or graphene on the crystallization of polymer: a small amount of nanofiller is sufficient to provide nucleation sites for polymer crystallization, whereas the nanoconfinement becomes the overwhelming factor when further increase the nanofiller concentration. In the present PE/RGO system, within the range of RGO loading studied, the crystallization rate of PE increases continuously with increasing the RGO content, which can be ascribed as the nucleation ability induced by the 2D sheets overcomes the nanoconfinement effects.

The Avrami equation⁴⁶ was employed to study the crystallization kinetics of PGNs as follows.

$$1 - X(t) = \exp(-Kt^n)$$

where $X(t)$ is the relative crystallinity calculated as the ratio of the heat of fusion at time t and the total heat of fusion of the whole crystallization process; n is the Avrami exponent and K is crystallization rate parameter. Twenty points were collected between 0% and 100% of the relative crystallinity $X(t)$. Figure 11a shows a representative Avrami plot of 0.2 vol % PGN. Values of n and K are determined using the initial linear part of the Avrami plot. The kinetics parameter K for PGNs at different isothermal crystallization temperatures are plotted in Figure 11b. Results of PGNs with high RGO loadings were not included in Figure 11 since the crystallization occurs so fast that no well-defined isothermal peaks can be obtained. It can be seen that for all PGNs in the temperature region studied K decreases with increasing crystallization temperature, which indicates the crystallization rate decreases at higher crystallization temperature. At the same crystallization temperature, K increases substantially with the increase of RGO contents and is

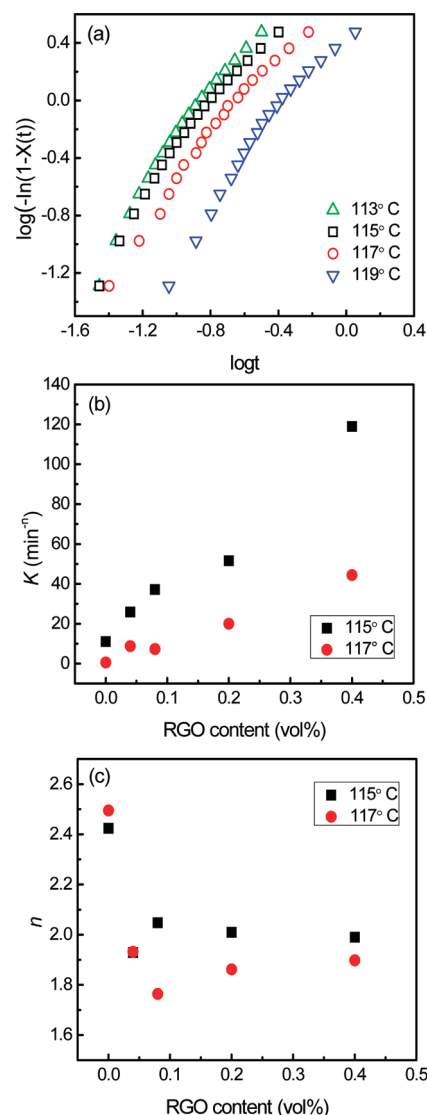


Figure 11. Avrami analysis of PGNs. (a) Avrami plot of isothermally crystallized 0.2 vol % PGN at different temperatures. (b) Effect of RGO contents on the crystallization rate parameter K at different isothermal crystallization temperatures. (c) Plot of Avrami exponent n as a function of RGO contents at different isothermal crystallization temperatures.

1–2 orders of magnitude higher at 0.4 vol % RGO loading compared with neat PE.

The Avrami exponent n typically indicates the growth dimension of the polymer. However, it should be noted that, in addition to growth dimensionality, the exponent also depends on many other factors. For example, 3D growth of athermal nucleation leads to an exponent of 3 while similar 3D growth of thermal nucleation has an exponent of 4. Other factors complicate the situation include volume change during crystallization, changing growth rate during crystal growth, changing of nucleation mechanism during crystallization due to exhaustion of the heterogeneous nuclei, etc.⁴⁷ Crystallization of PE melting may have an exponent of 1–4.⁴⁷ Therefore, caution should be taken when applying Avrami analysis in polymer crystallization. Nevertheless, general trends can normally be obtained when comparing the Avrami exponent of polymer nanocomposites with pristine polymers. For example, it has been reported that addition of 1 wt % CNT changes the n value

of PE ~ 2.5 to 1.6 .²⁸ A similar result is found for the PE/clay system, where the Avrami exponent is between 1 and 2 for nanocomposites samples.³² In the present case, the Avrami exponent decreases from 2.5 to 1.93 at 0.04 vol % of RGO loading and remains constant between 1.8 and 2 when further increasing the RGO content (Figure 11). Considering PE spherulite growth from a RGO surface, the growth dimensionality of individual spherulites may remain unchanged. However, such numerous spherulites would grow at or near the RGO surface, impinge with each other at a relatively early stage of crystallization, and form a quasi-2D layer of spherulites. Therefore, the observed Avrami exponent is decreased. Note that this decreased Avrami exponent should not suggest the change of growth behavior of individual crystals, but rather the dimensionality change of the overall growth (or solidification) process. This is consistent with PLM observation that the PE spherulite size is significantly reduced due to the impingement of adjacent spherulites at a relatively early stage of crystallization.

Thermal Stability of PGNs. The thermal stability of PGNs was evaluated by TGA under a nitrogen atmosphere (Figure

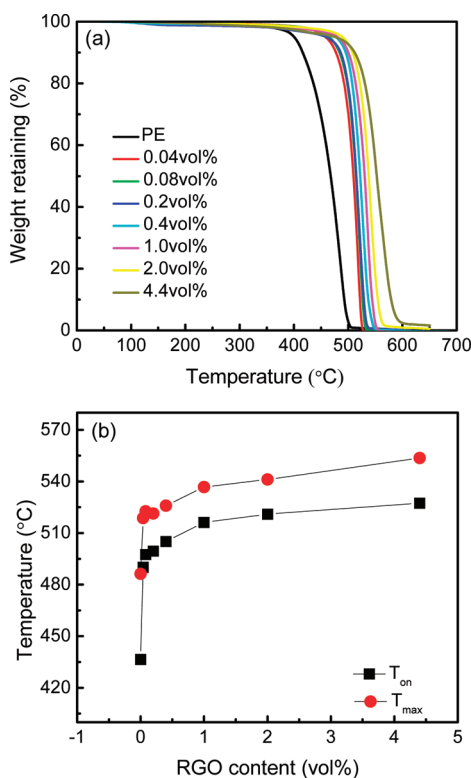


Figure 12. (a) TGA of PGNs. (b) Plot of degradation temperature vs RGO contents.

12). The temperature of the onset of degradation (T_{on}) and the temperature of maximum weight loss (T_{max}) for neat PE were recorded as 436.46 and 486.35 °C, respectively. Inclusion of as low as 0.04 vol % RGO sheets led to a 53.66 °C increase of T_{on} and a 32.38 °C increase of T_{max} . Further increasing RGO content gradually shifted the degradation temperature of the polymer to higher temperature. A 90.97 °C increase of T_{on} and a 67.33 °C increase of T_{max} were observed for 4.4 vol % PGN. This substantial enhancement of thermal stability can be ascribed to the high efficiency of the RGO to capture free radicals generated by polymer chain scission during the

degradation process at high temperature. The result is comparable with the PE/CNT system, where 65–115 °C increase of the degradation temperature was found at low CNT loading.²⁴ The observation suggests that although there are numerous defect sites on RGO, it is efficient in catching free radicals and improve the thermal stability of PE.

CONCLUSIONS

Solution crystallization was used to clearly reveal RGO-induced PE epitaxial crystallization. Small rodlike PE nuclei are randomly distributed on the basal plane of the RGO nanosheets at the initial crystallization stage and further grow into larger lamellae with average length of hundreds of nanometers. SAED shows that the polymer chain is parallel to the basal plane of the RGO sheets with an epitaxial relation $(0001)\langle 2-1-10 \rangle_{RGO} // (110)\langle 001 \rangle_{PE}$. A series of PGNs were fabricated via the solution crystallization/precipitation method. RGO was found to be uniformly dispersed in PE matrix, and the crystallization behavior of PE was significantly altered by addition of RGO. Crystallization shifts to higher temperature during cooling and the crystallization kinetics are much faster for all PGNs compared with neat PE, indicating the superb capability of RGO nanosheets to induce heterogeneous crystallization of PE. Decrease of Avrami exponent n was observed for PGNs, which was attributed to the RGO templating effect and relatively early impingement of PE crystals in the nanocomposite systems. Thermal stability of PGNs is also dramatically enhanced compared with neat PE due to the efficient charge transfer of the free radical generated by polymer chain scission to RGO.

AUTHOR INFORMATION

Corresponding Author

*E-mail: chrisli@drexel.edu; Tel 215-895-2083; Fax 215-895-6760.

ACKNOWLEDGMENTS

This work was supported by the National Science Foundation Grants DMR-0804838 (C.Y.L.), CMMI-1100166 (C.Y.L.), and CMMI-0825195 (Y.G.H.).

REFERENCES

- (1) Novoselov, K. S.; Geim, A. K.; Morozov, S. V.; Jiang, D.; Zhang, Y.; Dubonos, S. V.; Grigorieva, I. V.; Firsov, A. A. *Science* **2004**, 306, 666–669.
- (2) Du, X.; Skachko, I.; Barker, A.; Andrei, E. Y. *Nature Nanotechnol.* **2008**, 3, 491–495.
- (3) Peres, N. M. R.; Guinea, F.; Neto, A. H. C. *Phys. Rev. B* **2006**, 73, 125411.
- (4) Balandin, A. A.; Ghosh, S.; Bao, W. Z.; Calizo, I.; Teweldebrhan, D.; Miao, F.; Lau, C. N. *Nano Lett.* **2008**, 8, 902–907.
- (5) Ghosh, S.; Calizo, I.; Teweldebrhan, D.; Pokatilov, E. P.; Nika, D. L.; Balandin, A. A.; Bao, W.; Miao, F.; Lau, C. N. *Appl. Phys. Lett.* **2008**, 92, 151911.
- (6) Lee, C.; Wei, X. D.; Kysar, J. W.; Hone, J. *Science* **2008**, 321, 385–388.
- (7) Dikin, D. A.; Stankovich, S.; Zimney, E. J.; Piner, R. D.; Dommett, G. H. B.; Evmenenko, G.; Nguyen, S. T.; Ruoff, R. S. *Nature* **2007**, 448, 457–460.
- (8) Kim, H.; Abdala, A. A.; Macosko, C. W. *Macromolecules* **2010**, 43, 6515–6530.
- (9) Stankovich, S.; Dikin, D. A.; Dommett, G. H. B.; Kohlhaas, K. M.; Zimney, E. J.; Stach, E. A.; Piner, R. D.; Nguyen, S. T.; Ruoff, R. S. *Nature* **2006**, 442, 282–286.

- (10) Liang, J.; Huang, Y.; Zhang, L.; Wang, Y.; Ma, Y.; Guo, T.; Chen, Y. *Adv. Funct. Mater.* **2009**, *19*, 2297–2302.
- (11) Yang, X.; Li, L.; Shang, S.; Tao, X.-m. *Polymer* **2010**, *51*, 3431–3435.
- (12) Salavagione, H. J.; Martinez, G.; Gomez, M. A. *J. Mater. Chem.* **2009**, *19*, 5027–5032.
- (13) Steurer, P.; Wissert, R.; Thomann, R.; Mulhaupt, R. *Macromol. Rapid Commun.* **2009**, *30*, 316–327.
- (14) Xu, J. Z.; Chen, T.; Yang, C. L.; Li, Z. M.; Mao, Y. M.; Zeng, B. Q.; Hsiao, B. S. *Macromolecules* **2010**, *43*, 5000–5008.
- (15) Rafiee, M. A.; Rafiee, J.; Wang, Z.; Song, H. H.; Yu, Z. Z.; Koratkar, N. *ACS Nano* **2009**, *3*, 3884–3890.
- (16) Wang, S. R.; Tambraparni, M.; Qiu, J. J.; Tipton, J.; Dean, D. *Macromolecules* **2009**, *42*, 5251–5255.
- (17) Kim, H.; Miura, Y.; Macosko, C. W. *Chem. Mater.* **2010**, *22*, 3441–3450.
- (18) Khan, U.; May, P.; O'Neill, A.; Coleman, J. N. *Carbon* **2010**, *48*, 4035–4041.
- (19) Vickery, J. L.; Patil, A. J.; Mann, S. *Adv. Mater.* **2009**, *21*, 2180–2184.
- (20) Ramanathan, T.; Abdala, A. A.; Stankovich, S.; Dikin, D. A.; Herrera-Alonso, M.; Piner, R. D.; Adamson, D. H.; Schniepp, H. C.; Chen, X.; Ruoff, R. S.; Nguyen, S. T.; Aksay, I. A.; Prud'homme, R. K.; Brinson, L. C. *Nature Nanotechnol.* **2008**, *3*, 327–331.
- (21) Yan, J.; Wei, T.; Shao, B.; Fan, Z. J.; Qian, W. Z.; Zhang, M. L.; Wei, F. *Carbon* **2010**, *48*, 487–493.
- (22) Wang, D. W.; Li, F.; Zhao, J. P.; Ren, W. C.; Chen, Z. G.; Tan, J.; Wu, Z. S.; Gentle, I.; Lu, G. Q.; Cheng, H. M. *ACS Nano* **2009**, *3*, 1745–1752.
- (23) Li, G. L.; Liu, G.; Li, M.; Wan, D.; Neoh, K. G.; Kang, E. T. *J. Phys. Chem. C* **2010**, *114*, 12742–12748.
- (24) Kodjie, S. L.; Li, L. Y.; Li, B.; Cai, W. W.; Li, C. Y.; Keating, M. J. *Macromol. Sci., Phys.* **2006**, *45*, 231–245.
- (25) Li, L. Y.; Li, C. Y.; Ni, C. Y.; Rong, L. X.; Hsiao, B. *Polymer* **2007**, *48*, 3452–3460.
- (26) Li, C. Y.; Li, L. Y.; Cai, W. W.; Kodjie, S. L.; Tenneti, K. K. *Adv. Mater.* **2005**, *17*, 1198–1202.
- (27) Czerw, R.; Guo, Z. X.; Ajayan, P. M.; Sun, Y. P.; Carroll, D. L. *Nano Lett.* **2001**, *1*, 423–427.
- (28) Haggenueller, R.; Fischer, J. E.; Winey, K. I. *Macromolecules* **2006**, *39*, 2964–2971.
- (29) Cadek, M.; Coleman, J. N.; Barron, V.; Hedicke, K.; Blau, W. J. *Appl. Phys. Lett.* **2002**, *81*, 5123–5125.
- (30) Liu, T. X.; Phang, I. Y.; Shen, L.; Chow, S. Y.; Zhang, W. D. *Macromolecules* **2004**, *37*, 7214–7222.
- (31) Fornes, T. D.; Paul, D. R. *Polymer* **2003**, *44*, 3945–3961.
- (32) Gopakumar, T. G.; Lee, J. A.; Kontopoulou, M.; Parent, J. S. *Polymer* **2002**, *43*, 5483–5491.
- (33) Ke, Y. C.; Long, C. F.; Qi, Z. N. *J. Appl. Polym. Sci.* **1999**, *71*, 1139–1146.
- (34) Priya, L.; Jog, J. P. *J. Polym. Sci., Part B: Polym. Phys.* **2002**, *40*, 1682–1689.
- (35) Xu, J. Z.; Chen, C.; Wang, Y.; Tang, H.; Li, Z. M.; Hsiao, B. S. *Macromolecules* **2011**, *44*, 2808–2818.
- (36) Kim, H.; Kobayashi, S.; AbdurRahim, M. A.; Zhang, M. L. J.; Khushainova, A.; Hillmyer, M. A.; Abdala, A. A.; Macosko, C. W. *Polymer* **2011**, *52*, 1837–1846.
- (37) Li, Y. *Polymer* **2011**, *52*, 2310–2318.
- (38) Hummers, W. S.; Offerman, R. E. *J. Am. Chem. Soc.* **1958**, *80*, 1339.
- (39) Stankovich, S.; Dikin, D. A.; Piner, R. D.; Kohlhaas, K. A.; Kleinhammes, A.; Jia, Y.; Wu, Y.; Nguyen, S. T.; Ruoff, R. S. *Carbon* **2007**, *45*, 1558–1565.
- (40) Park, S.; An, J. H.; Jung, I. W.; Piner, R. D.; An, S. J.; Li, X. S.; Velamakanni, A.; Ruoff, R. S. *Nano Lett.* **2009**, *9*, 1593–1597.
- (41) Balik, C. M.; Tripathy, S. K.; Hopfinger, A. J. *J. Polym. Sci., Part B: Polym. Phys. Ed.* **1982**, *20*, 2003–2016.
- (42) Sano, M.; Sasaki, D. Y.; Kunitake, T. *Science* **1992**, *258*, 441–443.
- (43) Tuinstra, F.; Baer, E. *J. Polym. Sci., Part B: Polym. Lett.* **1970**, *8*, 861–865.
- (44) Takenaka, Y.; Miyaji, H.; Hoshino, A.; Tracz, A.; Jeszka, J. K.; Kucinska, I. *Macromolecules* **2004**, *37*, 9667–9669.
- (45) Dillon, D. R.; Tenneti, K. K.; Li, C. Y.; Ko, F. K.; Sics, I.; Hsiao, B. S. *Polymer* **2006**, *47*, 1678–1688.
- (46) Avrami, M. *J. Chem. Phys.* **1939**, *7*, 1103–1112.
- (47) Wunderlich, B. *Macromolecular Physics*; Academic Press: New York, 1976; Vol. II.